

## Constraining the Supernova Remnant Environment of FRB 190520B with Dispersion Measure and Scattering Timescale

JIA-PENG WEI,<sup>1</sup> CHEN DENG,<sup>2</sup> GWENael GIACINTI,<sup>3</sup> ZE-CHENG ZOU,<sup>2</sup> CHEN-RAN HU,<sup>2</sup> YONG-FENG HUANG,<sup>2,4</sup> AND JIN-JUN GENG<sup>5</sup>

<sup>1</sup>*Tsung-Dao Lee Institute, Shanghai Jiao Tong University, Shanghai 201210, P. R. China*

<sup>2</sup>*School of Astronomy and Space Science, Nanjing University, Nanjing 210023, China*

<sup>3</sup>*Université Paris Cité, CNRS, AstroParticule et Cosmologie, F-75013 Paris, France*

<sup>4</sup>*Key Laboratory of Modern Astronomy and Astrophysics (Nanjing University), Ministry of Education, China*

<sup>5</sup>*Purple Mountain Observatory, Chinese Academy of Sciences, Nanjing 210023, China*

### ABSTRACT

FRB 190520B is a repeating fast radio burst source whose large dispersion measure (DM) and temporal broadening suggest a dense and evolving local environment. In this work, we test the possibility that FRB 190520B originates from the core-collapse of a massive star so that its central engine is embedded in a supernova remnant (SNR) expanding into a wind environment, whose evolution is described by the self-similar solution. We use the observed DM and scattering timescale of FRB 190520B to constrain the physical parameters of its surrounding SNR and host-galaxy DM. Twenty typical cases are considered, arising from four ejecta profiles and five scattering prescriptions. It is found that only 6 cases are retained and provide acceptable fits. All retained cases have a shallow ejecta profile and a young source age of  $t_0 = 79.8\text{--}169.8$  yr. The ejecta mass is inferred to be large for all six cases, while the kinetic energy and mass-loss rate span a wide range. The secular DM evolution is reproduced better than the detailed scattering evolution. The up-drift behavior of the scattering residual suggests an additional component or more complicated structures inside the SNR. All retained cases are self-consistent within the adopted scattering theory and the circum-burst medium becomes transparent for GHz bursts before the inferred source ages.

*Keywords:* Interstellar medium (847) — Supernova remnants (1667) — Radio bursts (1339) — Radio transient sources (2008) — Compact radiation sources (289)

### 1. INTRODUCTION

Fast radio bursts (FRBs) are energetic radio transients with millisecond durations, originating from the deep sky (Lorimer et al. 2007). Their extremely high brightness temperatures strongly suggest a coherent emission mechanism (Zhang 2023). The observed dispersion measures (DMs) of FRBs are generally larger than the Galactic contribution estimated by the NE2001 model, providing compelling evidence for their extragalactic origin (Cordes & Lazio 2002; Thornton et al. 2013; Spitler et al. 2014, 2016; Niu et al. 2022). Recently, the Canadian Hydrogen Intensity Mapping Experiment (CHIME) reported more than 3600 newly detected FRBs in CHIME/FRB Catalog 2, bringing the total number of known FRB sources to over 4500 (CHIME/FRB Collaboration et al. 2026). Observationally, FRB sources are commonly divided into two categories: repeaters and apparent non-repeaters (Thornton et al. 2013; Spitler et al. 2016). There are several differences between the two populations in observa-

Corresponding author: Gwenaël Giacinti  
ggiacinti@apc.in2p3.fr

Corresponding author: Yong-Feng Huang  
hyf@nju.edu.cn

tions such as the time-frequency down-drifting behavior and the association with persistent radio sources (PRs) for repeaters (Chatterjee et al. 2017; Ricci et al. 2021; Niu et al. 2022).

Despite rapid observational progresses, the origin of FRBs remains under debate. Researchers have proposed many theoretical models, trying to explain the mechanisms responsible for FRBs (Geng & Huang 2015; Dai et al. 2016; Zhang 2017; Lyubarsky 2020; Beloborodov 2020). Convincing support for magnetars as FRB progenitors came from the discovery of FRB 200428, which was associated with the Galactic magnetar SGR 1935+2154 (Bochenek et al. 2020; CHIME/FRB Collaboration et al. 2020). Magnetars can be produced through at least two distinct evolutionary channels: the core-collapse of massive stars and compact binary mergers (Yoon et al. 2007; Giacomazzo & Perna 2013; Zhong & Dai 2020; Vink 2020). In both formation channels, an explosive event launches rapidly expanding ejecta and initiates the ejecta-dominated (ED) phase of remnant evolution. Because the ejecta expands supersonically into the ambient medium, a forward shock is formed and propagates outward, while a reverse shock is driven back into the ejecta by the pressure of the shocked ambient material (Truelove & McKee 1999, hereafter TM99). The shocked ejecta and shocked ambient medium are separated by a contact discontinuity (CD), across which the density and temperature generally change sharply (TM99). The hydrodynamical evolution of such systems has been extensively studied in the context of supernova remnants (SNRs). Self-similar solutions for SNR evolution were developed by Chevalier (1982) and Nadezhin (1985), in which the ejecta density profile is described by a uniform-density core and a power-law envelope. The structure of a SNR in the self-similar solution is shown in Figure 1, where  $R_{\text{core}}$ ,  $R_r$ ,  $R_c$ , and  $R_b$  are the radii of the core, reverse shock, CD shell, and forward shock, respectively.

FRB 190520B is a particularly intriguing source because of its exceptionally large DM of  $\sim 10^3$  pc cm $^{-3}$  and its extreme, time-variable rotation measure (RM), which has exhibited two sign reversals (Niu et al. 2022, 2026; Anna-Thomas et al. 2023). The source is localized to a star-forming region within a dwarf galaxy at a redshift of  $\sim 0.241$  and is associated with a PRS, showing remarkable similarities to FRB 121102 (Chatterjee et al. 2017; Tendulkar et al. 2017; Niu et al. 2022). It is well known that the radio emissions are dispersed and scattered as they pass through a plasma medium, resulting in a frequency-dependent delay in arrival time and temporal pulse broadening. Before reaching the Earth, FRB signals may traverse several media, including the interstellar medium (ISM) of the Milky Way, the intergalactic medium (IGM), the ISM of the host galaxy, and the local environment of the source.

In this work, we model the local environment of FRB 190520B as a SNR described by the self-similar solution, with a core-collapse massive-star progenitor, and consider several prescriptions for temporal broadening induced by plasma density fluctuations (Rickett 1977, 1990; Xu & Zhang 2016). Combining with the observed DMs and scattering timescales, we constrain the properties of the local environment and source system, including the ejecta mass, ejecta kinetic energy, and the mass-loss rate of the progenitor, as well as the source age and the DM contribution from its host galaxy. Compared with using DM alone, the joint consideration of DM and scattering timescale can provide tighter and more informative constraints on the SNR model. For the compact binary merger scenario, the evolutions of DM and RM have been investigated by Zhao et al. (2021). We assume that the observed DM includes contributions from all media along the line of sight, whereas the observed scattering timescale is dominated by the local SNR environment, with contributions from other regions being negligible (Luan & Goldreich 2014; Katz 2016), which will be discussed later.

This paper is organized as follows. In Section 2, we describe the self-similar SNR model and its dynamical evolution. Section 3 introduces the theoretical framework of temporal broadening induced by plasma density irregularities. In Section 4, we present the Bayesian inference and the Markov Chain Monte Carlo (MCMC) fitting procedure. The numerical results are given in Section 5. Finally, discussions and summary are provided in Sections 6 and 7.

## 2. THE SELF-SIMILAR SOLUTION OF SNR

The evolution of a SNR is commonly divided into four phases (Vink 2020): (i) the ED phase, during which the swept-up ambient mass is negligible compared with the ejecta mass and the ejecta expands approximately homogeneously; (ii) the Sedov–Taylor (ST) phase, when the swept-up mass becomes comparable to and even larger than the ejecta mass; (iii) the radiative or

snowplow phase; and (iv) the merging phase, in which the remnant gradually dissipates into the ambient medium. In this work, we focus exclusively on the ED phase, although our approximate solutions are also valid for the ST phase.

### 2.1. Characteristic scales

Following [TM99](#), the hydrodynamical evolution can be conveniently described by using dimensionless variables constructed from the ejecta mass, kinetic energy, and the normalization of the ambient density. The ambient medium is assumed to follow a density profile  $\rho_a = \eta_s r^{-s}$ , where  $\eta_s$  is a constant and  $s$  is the power-law index ([TM99](#)). To simplify the subsequent expressions, we define three characteristic scales from these independent parameters, i.e. the characteristic mass, length, and time as given by

$$M_{\text{ch}} = M_{\text{ej}}, \quad (1)$$

$$R_{\text{ch}} = M_{\text{ej}}^{1/(3-s)} \eta_s^{-1/(3-s)}, \quad (2)$$

$$t_{\text{ch}} = E_k^{-1/2} M_{\text{ej}}^{(5-s)/[2(3-s)]} \eta_s^{-1/(3-s)}. \quad (3)$$

In Section 2.3 below, a physical quantity  $X$  normalized by these characteristic scales is denoted as  $X^*$ , i.e.,  $X^* = X/M_{\text{ch}}^{x_1} R_{\text{ch}}^{x_2} t_{\text{ch}}^{x_3}$ , where  $x_1$ ,  $x_2$ , and  $x_3$  are constants determined by dimensional analysis.

Since we focus on the core-collapse scenario, the progenitor is naturally assumed to be embedded in a stellar wind environment. For a wind environment, we have  $s = 2$  and  $\eta_s = \dot{M}_w/4\pi v_w$ , where  $\dot{M}_w$  is the mass-loss rate of the progenitor and  $v_w$  is the wind velocity. The characteristic length and time are then given by

$$R_{\text{ch}} = 12.9 \text{ pc} \left( \frac{M_{\text{ej}}}{M_{\odot}} \right) \left( \frac{10^{-5} M_{\odot} \text{ yr}^{-1}}{\dot{M}_w} \right) \left( \frac{v_w}{10 \text{ km s}^{-1}} \right), \quad (4)$$

$$t_{\text{ch}} = 1772 \text{ yr} \left( \frac{10^{51} \text{ erg}}{E_k} \right)^{1/2} \left( \frac{M_{\text{ej}}}{M_{\odot}} \right)^{3/2} \left( \frac{10^{-5} M_{\odot} \text{ yr}^{-1}}{\dot{M}_w} \right) \left( \frac{v_w}{10 \text{ km s}^{-1}} \right). \quad (5)$$

### 2.2. Initial conditions

Following [TM99](#), the density profiles of the ejecta  $\rho_{\text{ej}}$  and the ambient medium  $\rho_a$  can be expressed as

$$\rho(r, t) = \begin{cases} \rho_{\text{ej}}(r, t) = \frac{M_{\text{ej}}}{R_{\text{ej}}^3} f\left(\frac{r}{R_{\text{ej}}}\right), & r \leq R_{\text{ej}}, \\ \rho_a = \eta_s r^{-s}, & r > R_{\text{ej}}, \end{cases} \quad (6)$$

where  $f\left(\frac{r}{R_{\text{ej}}}\right)$  is the structure function of ejecta, and  $R_{\text{ej}}$  is the outer layer radius of the ejecta. The structure function is assumed to follow a broken power-law profile ([TM99](#); [Zhao et al. 2021](#))

$$f(w) = \begin{cases} f_0, & 0 \leq w \leq w_{\text{core}}, \\ f_n w^{-n}, & w_{\text{core}} \leq w \leq 1, \end{cases} \quad (7)$$

where  $w = r/R_{\text{ej}}$ ,  $w_{\text{core}} = R_{\text{core}}/R_{\text{ej}}$ ,  $f_n = f_0 w_{\text{core}}^n$ , and  $n$  is the power-law index of the envelope of ejecta density. For  $s = 2$ , when  $n < 3$ , the ejecta profile contains no flat core so that  $w_{\text{core}} = 0$ . In this case the first branch of Equation (7) vanishes, and the ejecta profile reduces to a single power law,  $f(w) = f_n w^{-n}$  for  $0 \leq w \leq 1$ ; when  $n > 3$ , a finite core is present and we adopt a fiducial value  $w_{\text{core}} = 0.1$  following [Tang & Chevalier \(2017\)](#). The ejecta mass is conserved during the ED phase. Using mass conservation, the two normalization factors,  $f_n$  and  $f_0$ , can be written as ([TM99](#))

$$f_n = \frac{3-n}{4\pi}, \quad n < 3, \quad (8a)$$

$$f_0 = \frac{3}{4\pi w_{\text{core}}^n} \left[ \frac{1-(n/3)}{1-(n/3)w_{\text{core}}^{3-n}} \right], \quad n > 3. \quad (8b)$$

### 2.3. Approximate solutions of SNR

During the ED phase, two classes of approximate solutions can be obtained, depending on the power-law index  $n$  of the ejecta envelope. If the envelope is shallow ( $n < 5$ ), the solution is referred to as the free-expansion (FE) solution. If the envelope is steep ( $n > 5$ ), the corresponding solution is the self-similar driven wave (SSDW) solution. In this work, we consider the ejecta density profiles with  $n = 2, 4, 6$ , and  $8$ , which span both the shallow-envelope ( $n < 5$ , FE) and steep-envelope ( $n > 5$ , SSDW) regimes. We again emphasize that we focus on the core-collapse scenario, corresponding to  $s = 2$ . This means that the values of some parameters involved in the approximate solutions, which will be presented later, are only valid for the scenario of  $s = 2$ .

For the FE solution, following [Tang & Chevalier \(2017\)](#), the evolution of the reverse shock, CD shell, and forward shock is characterized by

$$R_r^* = q_r R_c^*, \quad (9)$$

$$R_c^* = \left[ (\lambda_c t^*)^{-a} + (c t^{*b})^{-a} \right]^{-1/a}, \quad (10)$$

$$R_b^*(t^*) = \left[ (\lambda_b t^*)^{-2\alpha} + (\xi t^{*2})^{-2\alpha/(5-s)} \right]^{-1/(2\alpha)}, \quad (11)$$

where  $q_r = q_b/l_{ED}$ , with  $q_b = 1.19$  and

$$l_{ED} = 1 + \frac{8}{n^2} + \frac{0.4}{4-s}. \quad (12)$$

The parameters of  $\lambda_c$ ,  $\lambda_b$ , and  $\xi$  are given by [Tang & Chevalier \(2017\)](#) as,

$$\lambda_c = \begin{cases} [2(\frac{5-n}{3-n})]^{1/2}, & n < 3, \\ [2w_{core}^{-2}(\frac{5-n}{3-n})(\frac{w_{core}^{n-3}-n/3}{w_{core}^{n-5}-n/5})]^{1/2}, & n > 3, \end{cases} \quad (13)$$

with  $\lambda_b = q_b \lambda_c$  and  $\xi = 3/2\pi$ . The parameters  $a$ ,  $b$ ,  $c$ , and  $\alpha$  depend on the ejecta power-law index  $n$  and the ambient density profile  $s$ , and their numerical values are tabulated in Tables 4 and 6 of [Tang & Chevalier \(2017\)](#). We further introduce the transition time  $t_{tran}^*$ , which marks the end of the ED phase and the onset of the ST phase. In the FE solution, the transition time can be expressed as ([Tang & Chevalier 2017](#))

$$t_{tran}^* = \left( \frac{\xi}{\lambda_b^{5-s}} \right)^{1/(3-s)}. \quad (14)$$

For the SSDW solution, the CD shell and forward shock evolve as ([Tang & Chevalier 2017](#))

$$R_c^* = \left[ (\zeta_c t^{*(n-3)/(n-s)})^{-a} + (c t^{*b})^{-a} \right]^{-1/a}, \quad (15)$$

$$R_b^*(t^*) = \left[ (\zeta_b t^{*(n-3)/(n-s)})^{-\alpha} + (\xi t^{*2})^{-\alpha/(5-s)} \right]^{-1/\alpha}, \quad (16)$$

where  $\zeta_c$  and  $\zeta_b$  are also tabulated in Tables 4 and 6 of [Tang & Chevalier \(2017\)](#). The evolution of the reverse shock in this case is more complicated and is divided into two regimes by the time  $t_{core}^*$ , when the reverse shock reaches the flat core ([Micelotta et al. 2016](#)). This timescale is given by ([Hwang & Laming 2012](#); [Micelotta et al. 2016](#))

$$t_{core}^* = \left[ \frac{l_{ED}^{s-2}}{\phi_{ED}} \frac{3(3-s)^2}{4\pi n(n-3)} \right]^{1/(3-s)} \frac{1}{v_{core}^*}, \quad (17)$$

where

$$\phi_{ED} = (0.65 - \exp(-n/4)) \sqrt{1 - \frac{s}{8}}. \quad (18)$$

Before the reverse shock hits the core (i.e.  $t^* < t_{core}^*$ ), the reverse shock radius is ([Micelotta et al. 2016](#))

$$R_r^* = \left\{ v_{core}^* \frac{(n-3)(3-s)^2}{n(n-3)} \frac{3}{4\pi} \frac{l_{ED}^{n-2}}{\phi_{ED}} \right\}^{\frac{1}{n-s}} \frac{t^{*\frac{n-3}{n-s}}}{l_{ED}}. \quad (19)$$

When  $t^* > t_{\text{core}}^*$ , the self-similar description of the ejecta structure breaks down because the reverse shock has penetrated into the flat core. Following [Laming & Hwang \(2003\)](#) and [Micelotta et al. \(2016\)](#), we approximate the forward shock radius and velocity entering the post-core reverse shock solution by their values at  $t^* = t_{\text{core}}^*$ . Under this prescription, the reverse-shock radius for  $t^* > t_{\text{core}}^*$  can be written as

$$R_r^*(t^*) = \left[ \frac{R_b^*(t_{\text{core}}^*)}{l_{\text{ED}} t_{\text{core}}^*} - \frac{3-s}{n-3} \frac{v_b^*(t_{\text{core}}^*)}{l_{\text{ED}}} \ln \left( \frac{t^*}{t_{\text{core}}^*} \right) \right] t^*. \quad (20)$$

For the SSDW solution, the transition time is ([Tang & Chevalier 2017](#))

$$t_{\text{tran}}^* = \left( \frac{\xi}{\xi_b^{5-s}} \right)^{(n-s)/[(n-5)(3-s)]}. \quad (21)$$

In the following, we use these solutions to model the time evolution of the DM contributed by different regions of the SNR.

#### 2.4. The evolution of DM

The observed DM consists of several components:

$$DM_{\text{obs}} = DM_{\text{MW}} + DM_{\text{MW,halo}} + DM_{\text{IGM}} + \frac{DM_{\text{host}} + DM_{\text{local}}}{1 + z_0}, \quad (22)$$

where  $z_0$  is the redshift of FRB source,  $DM_{\text{MW}}$ ,  $DM_{\text{MW,halo}}$ ,  $DM_{\text{IGM}}$ ,  $DM_{\text{host}}$ , and  $DM_{\text{local}}$  denote the contributions from the ISM of the Milky Way, the Galactic halo, the IGM, the ISM of host galaxy, and the local SNR environment, respectively. For FRB 190520B, following [Niu et al. \(2022\)](#), we adopt  $DM_{\text{MW}} = 113 \pm 17 \text{ pc cm}^{-3}$  and  $DM_{\text{IGM}} = 195_{-70}^{+110} \text{ pc cm}^{-3}$ . Since  $DM_{\text{MW,halo}}$  is expected to lie in the range  $30\text{--}80 \text{ pc cm}^{-3}$ , we adopt the midpoint value,  $55 \text{ pc cm}^{-3}$ , as the fiducial contribution and take half of the interval width as a symmetric uncertainty. This yields  $DM_{\text{MW,halo}} = 55 \pm 25 \text{ pc cm}^{-3}$ . In this work,  $DM_{\text{host}}$  is treated as a free parameter. The local contribution  $DM_{\text{local}}$  is further divided into four components from the SNR: the unshocked core ( $r < R_{\text{core}}$ ), the unshocked ejecta envelope ( $R_{\text{core}} < r < R_r$ ), the shocked ejecta ( $R_r < r < R_c$ ), and the shocked ambient medium ( $R_c < r < R_b$ ), as shown in [Figure 1](#).

When  $n < 3$ , there is no flat core and the unshocked ejecta extends to the center of SNR. To avoid the singularity of DM at the SNR center, we introduce a cutoff radius,  $R_{\text{cut}} = 0.01R_r$ . Therefore, the DM contribution from unshocked ejecta in this case is

$$DM_{\text{unsh,ej}} = \frac{M_{\text{ej}}}{\mu m_p} \eta f_n \frac{R_r^{1-n} - R_{\text{cut}}^{1-n}}{(1-n)R_c^{3-n}}, \quad (23)$$

where  $\eta$  is the ionization fraction,  $\mu$  is the mean atomic weight, and  $m_p$  is the proton mass. In this work, we take  $\mu \sim 1$  and  $\eta = 0.03$  ([Chevalier & Fransson 2017](#); [Zhao et al. 2021](#)). We also adopt  $R_{\text{ej}} \sim R_c$  in the ED phase, which is a reasonable approximation in the self-similar framework ([Chevalier 1982](#)). When  $n > 3$ , the DM contributions from the unshocked core and the unshocked ejecta are

$$DM_{\text{unsh,core}} = \frac{M_{\text{ej}}}{\mu m_p R_c^3} \eta f_0 R_{\text{core}}, \quad (24)$$

$$DM_{\text{unsh,ej}} = \frac{M_{\text{ej}}}{\mu m_p} \eta f_0 w_{\text{core}}^n \frac{R_r^{1-n} - R_{\text{core}}^{1-n}}{(1-n)R_c^{3-n}}. \quad (25)$$

The downstream density of a strong shock is compressed by 4 times ([Zhang 2018](#)). Accordingly, for the forward shock, the electron density in the shocked ambient medium is

$$n_{\text{e,a}} = 4n_0 = \frac{4\eta_s}{\mu m_p} r^{-s}, \quad (26)$$

where  $n_0$  is the density of the unshocked ambient medium. Under the thin-shell approximation, the electron density in the shocked ejecta is ([Chevalier 1982](#))

$$n_{\text{e,ej}} = \frac{(n-3)(n-4)}{(3-s)(4-s)} n_{\text{e,a}}. \quad (27)$$

The corresponding DM contributions from the shocked ejecta and the shocked ambient medium are then

$$DM_{\text{sh,ej}} = \frac{4\eta_s}{\mu m_p} \frac{(n-3)(n-4)}{(3-s)(4-s)} \frac{R_c^{1-s} - R_r^{1-s}}{1-s}, \quad (28)$$

$$DM_{\text{sh,a}} = \frac{4\eta_s}{\mu m_p} \frac{R_b^{1-s} - R_c^{1-s}}{1-s}. \quad (29)$$

### 3. TEMPORAL BROADENING OF RADIO PULSES IN TURBULENT PLASMA

We assume that the three-dimensional power spectrum of electron density irregularity in the turbulent plasma takes the form (Rickett 1977, 1990)

$$P_{3N}(k) = C_N^2(r) \left(k^2 + \left(\frac{2\pi}{L}\right)^2\right)^{-\beta/2} \exp\left(-k^2 / \left(\frac{2\pi}{l_0}\right)^2\right), \quad (30)$$

where  $k$  is the spatial wavenumber and  $\beta$  is the spectral index. Here,  $L$  and  $l_0$  are the outer and inner scales of turbulence, corresponding to the energy injection and dissipation scales, respectively (Xu & Zhang 2016).

Within the inertial range, Equation (30) reduces to

$$P_{3N}(k) = C_N^2(r) k^{-\beta}, \quad 2\pi/L \ll k \ll 2\pi/l_0. \quad (31)$$

Observations indicate that the spectral index  $\beta$  lies between 2 and 4 (Lee & Jokipii 1975a; Rickett 1977). From the normalization of the power-law spectrum,  $\int P_{3N}(k) d^3\vec{k} = (\delta n_e)^2$ , one obtains (Xu & Zhang 2016)

$$C_N^2 \simeq \begin{cases} \frac{\beta-3}{2(2\pi)^{4-\beta}} (\delta n_e)^2 L^{3-\beta}, & \beta > 3, \\ \frac{3-\beta}{2(2\pi)^{4-\beta}} (\delta n_e)^2 l_0^{3-\beta}, & \beta < 3, \end{cases} \quad (32)$$

where  $n_e$  is the number density of electrons,  $\delta n_e = n_e - \langle n_e \rangle$  is the root-mean-square (rms) amplitude of the density fluctuation, and  $\langle \rangle$  denotes an ensemble average in the radial direction. The case of  $\beta = 3$  is excluded, since in this situation  $\delta n_e$  becomes scale-independent (Xu & Zhang 2016).

When the radio waves propagate through a turbulent plasma, their pulse widths are broadened due to the multi-path scattering (Rickett 1990; Xu & Zhang 2016). The wave structure function,  $D_\phi$ , which represents the mean square phase difference between two points separated by  $\sigma_s$ , is given by (Rickett 1977; Yang et al. 2022)

$$D_\phi = \begin{cases} f_1 \pi^2 r_e^2 \lambda^2 C_N^2 \Delta D l_0^{\beta-4} \sigma_s^2, & \sigma_s < l_0, \\ f_2 \pi^2 r_e^2 \lambda^2 C_N^2 \Delta D \sigma_s^{\beta-2}, & \sigma_s > l_0, \end{cases} \quad (33)$$

where  $r_e$  is the classical electron radius,  $\lambda$  is the wavelength of the electromagnetic wave,  $\Delta D$  is the straight-line path through the turbulent plasma. The coefficients are  $f_1 = \Gamma(1 - \alpha/2)$ ,  $f_2 = [\Gamma(1 - \alpha/2)/\Gamma(1 + \alpha/2)] \frac{8}{\alpha^{2\alpha}}$ , and  $\alpha = \beta - 2$ . The approximation of  $\int C_N^2 dz \approx C_N^2 \Delta D$  is adopted. The diffractive length,  $\sigma_{\text{diff}}$ , is defined by the condition of  $D_\phi = 1$  rad. It then can be expressed as (Xu & Zhang 2016; Yang et al. 2022)

$$\sigma_{\text{diff}} = \begin{cases} (f_1 \pi^2 r_e^2 \lambda^2 C_N^2 \Delta D l_0^{\beta-4})^{-\frac{1}{2}}, & \sigma_{\text{diff}} < l_0, \\ (f_2 \pi^2 r_e^2 \lambda^2 C_N^2 \Delta D)^{\frac{1}{2-\beta}}, & \sigma_{\text{diff}} > l_0. \end{cases} \quad (34)$$

The angular broadening induced by the multi-path scattering is (Rickett 1990; Xu & Zhang 2016)

$$\theta_{\text{sc}} = \frac{1}{k \sigma_{\text{diff}}}. \quad (35)$$

The corresponding temporal broadening is given by (Lee & Jokipii 1975b)

$$\tau_{\text{sc}} = \frac{D \theta_{\text{sc}}^2}{2c}, \quad (36)$$

where  $D$  is the distance between the turbulent plasma and the source in the thin-screen case, while for a thick screen it denotes the propagation path length, and  $c$  is the speed of light. We include the cosmological correction and adopt  $\Delta D \sim D$  and  $DM \approx \delta n_e D$  (Xu & Zhang 2016; Yang et al. 2022). To account for clumpy density structures, we introduce the volume filling factor  $f = \langle n_e \rangle^2 / \langle n_e^2 \rangle$  and replace  $\delta n_e$  with  $\sqrt{f} \delta n_e$  (Xu & Zhang 2016).

For  $\beta < 3$ ,  $\tau_{\text{sc}}$  can be written as

$$\tau_{\text{sc}} = \frac{r_e^2 \lambda^4 DM^2}{16c(1+z_0)^3} \frac{f_1(3-\beta)}{(2\pi)^{4-\beta}} \left(\frac{\delta n_e}{n_e}\right)^2 f l_0^{-1}, \quad \sigma_{\text{diff}} < l_0, \quad (37a)$$

$$\tau_{\text{sc}} = \frac{r_e^{\frac{4}{\beta-2}} \lambda^{\frac{2\beta}{\beta-2}} DM^{\frac{\beta}{\beta-2}}}{8c\pi^{\frac{2(\beta-4)}{\beta-2}} (1+z_0)^{\frac{\beta+2}{\beta-2}}} \left(\frac{f_2(3-\beta)}{2(2\pi)^{4-\beta}}\right)^{\frac{2}{\beta-2}} \left(\frac{\delta n_e}{n_e}\right)^{\frac{\beta}{\beta-2}} (\delta n_e)^{\frac{4-\beta}{\beta-2}} f^{\frac{2}{\beta-2}} l_0^{\frac{2(3-\beta)}{\beta-2}}, \quad \sigma_{\text{diff}} > l_0. \quad (37b)$$

In Equation (37a),  $\beta$  affects only the numerical coefficient. We therefore fix  $\frac{f_1(3-\beta)}{(2\pi)^{4-\beta}}$  at its maximum value, 0.04. By contrast, in Equation (37b),  $\beta$  is treated as a free parameter. For  $\beta > 3$ ,  $\tau_{\text{sc}}$  can be written as

$$\tau_{\text{sc}} = \frac{r_e^2 \lambda^4 DM^2}{16c(1+z_0)^3} \frac{f_1(\beta-3)}{(2\pi)^{4-\beta}} \left(\frac{\delta n_e}{n_e}\right)^2 f \left(\frac{l_0}{L}\right)^{\beta-4} L^{-1}, \quad \sigma_{\text{diff}} < l_0, \quad (38a)$$

$$\tau_{\text{sc}} = \frac{r_e^{\frac{4}{\beta-2}} \lambda^{\frac{2\beta}{\beta-2}} DM^{\frac{\beta}{\beta-2}}}{8c\pi^{\frac{2(\beta-4)}{\beta-2}} (1+z_0)^{\frac{\beta+2}{\beta-2}}} \left(\frac{f_2(\beta-3)}{2(2\pi)^{4-\beta}}\right)^{\frac{2}{\beta-2}} \left(\frac{\delta n_e}{n_e}\right)^{\frac{\beta}{\beta-2}} (\delta n_e)^{\frac{4-\beta}{\beta-2}} f^{\frac{2}{\beta-2}} L^{\frac{2(3-\beta)}{\beta-2}}, \quad \sigma_{\text{diff}} > l_0. \quad (38b)$$

In this work, for  $\beta > 3$ , we adopt the Kolmogorov spectrum, i.e.  $\beta = 11/3$ .

Rickett (1977) suggested that a power-law spectrum with  $\beta \geq 4$  is observationally indistinguishable from a Gaussian spectrum. In addition, a spectral index of  $\beta = 4$  is expected when the line of sight passes through an abrupt structure in plasmas (Armstrong et al. 1995). Motivated by these considerations, we also include the Gaussian spectrum in this work. The corresponding temporal broadening is

$$\tau_{\text{sc}} = \frac{r_e^2 \lambda^4 DM^2}{4c\pi^{1/2}(1+z_0)^3} \left(\frac{\delta n_e}{n_e}\right)^2 f l_0^{-1}. \quad (39)$$

Its derivation follows essentially the same procedure as that for the power-law spectrum. A detailed derivation is presented in Appendix A.

For convenience, we assign simplified labels to the different expressions of  $\tau_{\text{sc}}$ : Equations (37a), (37b), (38a), (38b), and (39) are denoted as models A, B, C, D, and E, respectively. In this study, we consider ejecta envelopes with power-law indices  $n = 2, 4, 6$ , and 8. To distinguish models with different  $n$ , we append the value of  $n$  to the model label. For example, model A with  $n = 2$  is denoted as A2.

Before reaching the Earth, FRBs propagate through several media, including its local plasma, the host galaxy ISM, the IGM, and the Galactic ISM. Yang et al. (2022) reported that the scintillation bandwidths,  $\delta\nu_{\text{sc}}$ , of order  $\sim 1$  MHz observed in FRBs originate from the Milky Way. Using the uncertainty relation,  $2\pi\tau_{\text{sc}}\delta\nu_{\text{sc}} \sim 1$ , we estimate that the temporal broadening contributed by the Milky Way is of order  $10^{-4}$  ms, which is far below 1 ms. We therefore neglect the Galactic contribution to the observed temporal broadening. Xu & Zhang (2016) suggested that a spectral index  $\beta > 3$  is more likely in the IGM. For such a plasma to contribute significantly to temporal broadening, the outer scale  $L$  would need to be smaller than  $10^{-2}$  pc. However, Luan & Goldreich (2014) argued that, for a Kolmogorov spectrum, the outer scale in the IGM is generally larger than  $10^5$  pc. We thus consider the IGM contribution to be negligible. The host galaxies of FRB 121102A and FRB 190520B share remarkably similar properties, and bursts from FRB 121102A show no significant scattering tails (Li et al. 2021; Zhang 2023; Wei et al. 2025). It is therefore reasonable, as a working assumption, to neglect the contribution from the host galaxy of FRB 190520B as well. Accordingly, we attribute the observed temporal broadening primarily to the local environment of FRB 190520B. In this study, we model its local environment as a SNR comprising four components, as illustrated in Figure 1. Strong turbulence is expected to primarily arise from the shocked ejecta and the shocked ambient medium, driven by Rayleigh-Taylor instabilities (Shirkey 1978; Frascetti et al. 2010). We hence assume that the temporal broadening is produced mainly in the shocked ejecta

and shocked ambient medium. The observed scattering timescale is then treated as the convolution of the contributions from these two components.

We adopt the central frequency of the Five-hundred-meter Aperture Spherical radio Telescope (FAST),  $\nu = 1.25$  GHz, as the observing frequency of bursts from FRB 190520B. The DM contributions from the shocked ejecta and the shocked ambient medium, which are used separately in the calculation of  $\tau_{\text{sc}}$ , are given by Equations (28) and (29), respectively. According to their definitions, the rms density fluctuation  $\delta n_e$ , the electron number density  $n_e$ , and the volume filling factor  $f$  can be derived from Equations (26) and (27). Following Coles & Harmon (1989), the inner scale  $l_0$  for each model is determined by

$$l_0 = 3 \sqrt{\frac{m_p c}{4\pi e} n_e^{-1/2}}, \quad (40)$$

where  $e$  is the elementary charge. The quantities  $n_e$ ,  $\delta n_e$ , and  $l_0$  are all functions of both time and radius. Since we are interested in their temporal evolution, at each time slice we radially average the composite terms constructed from these quantities, as shown in scattering formalism. The outer scale  $L$  is obtained from a linear fit of simulation data and is given by (Dwarkadas 2000)

$$L = 0.037 t R_{\text{ch}}/t_{\text{ch}}, \quad (41)$$

where  $R_{\text{ch}}$  and  $t_{\text{ch}}$  are the characteristic length and time defined in Section 2.1.

It is worth noting that ISM-like environments essentially satisfy the three assumptions underlying the standard theory of temporal broadening (Rickett 1977): (i) the deviations of refractive index are much less than unity everywhere; (ii) the inner scale  $l_0$  is much larger than the wavelength of electromagnetic wave,  $\lambda$ ; and (iii) the outer scale  $L$  is much less than the thickness of medium. In this work, we extend these assumptions to the SNR environment. As shown in Section 6, our results suggest that, within the parameter space constrained in this work, these assumptions are satisfied in the SNR environment of FRB 190520B, thus validating the results derived from the scattering theory adopted here.

#### 4. BAYESIAN INFERENCE

Based on the theoretical framework of SNR evolution and the temporal broadening models introduced in Sections 2 and 3, we now adopt a Bayesian approach to constrain the physical parameters of the SNR of FRB 190520B and its host galaxy, using the observed DMs and scattering timescales.

The DM measurements are compiled from Niu et al. (2022, 2026) and Anna-Thomas et al. (2023), yielding a total of 646 data points, while the observed scattering timescales are taken from Niu et al. (2022, 2026), comprising 95 measurements. Niu et al. (2026) reported scattering timescales in three frequency bands centered at 1.075, 1.225, and 1.4 GHz. We take these central frequencies as the observing frequencies of the corresponding bursts and rescale the reported scattering timescales to the frequency of 1.25 GHz using the scaling law  $\tau_{\text{sc}} \propto \nu^{-4}$ . The rescaled scattering timescales from the three bands are then convolved to obtain the final scattering timescale for each burst reported in Niu et al. (2026).

We consider a wind environment with  $s = 2$  and ejecta envelopes characterized by power-law indices  $n = 2, 4, 6, \text{ or } 8$ , which determine the dynamical evolution of density profiles, shell radii, and DM contributions from different SNR regions. The free parameters in our model are the ejecta mass  $M_{\text{ej}}$ , kinetic energy  $E_k$ , progenitor mass-loss rate  $\dot{M}_w$ , the source age  $t_0$ , and the DM contribution from host galaxy  $DM_{\text{host}}$ . The wind velocity is fixed at  $v_w = 100 \text{ km s}^{-1}$ . For model B, the spectral index  $\beta$  is treated as an additional free parameter. The parameter  $t_0$  is defined as the source age, which also means at that time, the first observed burst from FRB 190520B was generated. Using the arrival time of individual bursts, the generated time of all observed bursts can be determined relative to  $t_0$ . Observationally,  $DM_{\text{host}}$  and  $DM_{\text{local}}$  are coupled. By treating  $DM_{\text{host}}$  as a free parameter,  $DM_{\text{local}}$  can be inferred from the observed  $DM_{\text{obs}}$  after subtracting the other contributions. Its uncertainty is obtained through standard error propagation,

$$\sigma_{\text{local}}^2 = (\sigma_{\text{obs}}^2 + \sigma_{\text{MW}}^2 + \sigma_{\text{halo}}^2 + \sigma_{\text{IGM}}^2) \times (1 + z_0)^2, \quad (42)$$

where  $\sigma_{\text{MW}}$ ,  $\sigma_{\text{halo}}$ , and  $\sigma_{\text{IGM}}$  are the uncertainties associated with the Milky Way, Galactic halo, and IGM contributions, respectively (see Section 2.4), and  $\sigma_{\text{obs}}$  is the uncertainty of the observed DM presented in Niu et al. (2022, 2026) and Anna-Thomas

et al. (2023). The factor  $(1 + z_0)^2$  accounts for the redshift correction when converting the uncertainties of the local DM contribution to the source frame.

We employ `scipy.optimize.minimize`<sup>1</sup> at first to obtain reasonable initial values for the free parameters. With these initial values, we then perform MCMC fitting to  $DM_{\text{local}}$  and scattering timescale data by using `emcee`<sup>2</sup>. In this work, we used the inferred  $DM_{\text{local}}$  in MCMC procedure, whereas  $DM_{\text{obs}}$  is adopted in subsequent discussion. The logarithmic likelihood functions for  $DM_{\text{local}}$  and  $\tau_{\text{sc}}$  adopted in MCMC are

$$\log \mathcal{L}_{DM_{\text{local}}} = -\frac{1}{2} \sum_i \left[ \left( \frac{DM_{\text{local},i} - \hat{DM}_{\text{local},i}}{\sigma_{DM_{\text{local},i}}} \right)^2 + \ln(2\pi\sigma_{DM_{\text{local},i}}^2) \right], \quad (43a)$$

$$\log \mathcal{L}_{\tau_{\text{sc}}} = -\frac{1}{2} \sum_i \left[ \left( \frac{\tau_{\text{sc},i} - \hat{\tau}_{\text{sc},i}}{\sigma_{\tau_{\text{sc},i}}} \right)^2 + \ln(2\pi\sigma_{\tau_{\text{sc},i}}^2) \right], \quad (43b)$$

where  $DM_{\text{local},i}$  and  $\tau_{\text{sc},i}$  are the inferred local DM and the observed scattering timescale for the  $i$ th data point, respectively, and  $\sigma_{DM_{\text{local},i}}$  and  $\sigma_{\tau_{\text{sc},i}}$  are their corresponding uncertainties. The quantities with hats denote the values predicted by theories. The total likelihood is taken as the sum of the two logarithmic likelihoods.

In this work, the transition time from the ED phase to the ST phase,  $t_{\text{tran}}$ , is required to be smaller than  $10^4$  yr. The prior ranges for  $M_{\text{ej}}$ ,  $E_{\text{k}}$ , and  $\dot{M}_{\text{w}}$  are set to  $1 - 20 M_{\odot}$ ,  $10^{50} - 10^{52}$  erg, and  $10^{-8} - 10^{-3} M_{\odot} \text{ yr}^{-1}$ , respectively (Smartt 2009; Smith 2014). Some previous studies suggested that  $t_0$  for FRB 190520B is of the order of a few decades, while Rahaman et al. (2025) argued that the persistent radio source of FRB 190520B has an age of 10 – 100 years (Wang et al. 2025; Bhattacharya et al. 2025). We therefore adopt a broader prior range of 10–200 yr for  $t_0$ . The prior range for  $DM_{\text{host}}$  is set to  $1 - 1000 \text{ pc cm}^{-3}$ , estimated by subtracting other contributions from the minimum observed DM in the source frame. For model B, the additional free parameter  $\beta$  is restricted to the range from  $2 + e^{-1}$  to 3. The lower limit is set as  $2 + e^{-1}$  to ensure it is sufficiently small and to avoid numerical instabilities in the calculations. Since we cannot constrain the entire evolution of SNR in the ED phase by observations spanning several years, we use the MCMC method to find the best-fit of free parameters. For the MCMC sampling, thereby, we run 10,000 steps with 48 walkers. No burn-in is considered, and thinning factor is set to 1.

## 5. NUMERICAL RESULTS

FRB 190520B is an intriguing repeating source, characterized by its large DMs, extreme and time-variable RM with two sign reversals, and its association with a PRS, all of which point to a complex and evolving local environment. In this section, we present the results obtained from the joint analysis of the DM and scattering timescale data of FRB 190520B. Combining the five prescriptions for temporal broadening with ejecta profiles of  $n = 2, 4, 6,$  and  $8$  yields 20 cases in total. Among them, we found that only six cases provide acceptable fits to both the DM and scattering timescale data, namely cases A2, A4, B2, B4, E2, and E4. Notably, all the six cases belong to the FE solution with  $n = 2$  or  $4$ , whereas none of the SSDW solution with  $n = 6$  or  $8$  is retained. This trend suggests that the current data favor shallower ejecta-density profiles. However steeper profiles with  $n > 8$  cannot be ruled out completely. The best-fit parameters for the six cases, together with the inferred transition times  $t_{\text{tran}}$ , are listed in Table 1.

The derived parameter values span a broad range. The ejecta masses are  $M_{\text{ej}} = 8.7\text{--}19.2 M_{\odot}$ , while the kinetic energies range from  $1 \times 10^{50}$  erg to  $7.3 \times 10^{51}$  erg. The inferred wind mass-loss rates are  $\dot{M}_{\text{w}} = 0.3\text{--}14.8 \times 10^{-5} M_{\odot} \text{ yr}^{-1}$ , and the source ages are  $t_0 = 79.8\text{--}169.8$  yr. Thus, all cases imply that FRB 190520B is embedded in a young, approximately century-old SNR environment. The DM contributions from host galaxy differ substantially among the cases. Cases A2, A4, B4, and E4 require extremely small host contributions,  $DM_{\text{host}} = 10.7\text{--}28.7 \text{ pc cm}^{-3}$ , whereas cases B2 and E2 require larger values of 998.0 and 407.6  $\text{pc cm}^{-3}$ , respectively. Cases B2 and B4 give the same best-fit turbulence spectral index,  $\beta = 2.9$ .

<sup>1</sup> <https://docs.scipy.org/doc/scipy/reference/generated/scipy.optimize.minimize.html>

<sup>2</sup> <https://emcee.readthedocs.io>

The corresponding fits to the observed DMs and their residuals are shown in Figure 2. One can see that, during the burst epoch, the DM evolution becomes nearly stable for B2, indicating that the observed DMs are primarily dominated by the contribution from the host galaxy. By contrast, other cases of A2, A4, B4, E2 and E4 still exhibit an obvious decreasing trend in DM at their burst epoch. Wang et al. (2025) reported a DM decrease of approximately  $11 \text{ pc cm}^{-3} \text{ yr}^{-1}$  with a significance above  $10\sigma$ , while Niu et al. (2026) obtained a decrease rate of  $12.4 \pm 0.3 \text{ pc cm}^{-3} \text{ yr}^{-1}$ . The DM slopes predicted by Cases A2, A4, B2, B4, E2, and E4 are  $-13.2$ ,  $-12.3$ ,  $-0.3$ ,  $-12.0$ ,  $-12.3$ , and  $-12.1 \text{ pc cm}^{-3} \text{ yr}^{-1}$ , respectively. Except for B2, the predicted slopes are broadly consistent with the observed DM decrease reported by Niu et al. (2026).

To illustrate the physical origin of the DM evolution, the contributions from different regions of the SNR are further illustrated via the gray dashed lines with different markers in Figure 2. As shown in Section 2, the presence of the ejecta core and the shocked ejecta is subjective to the value of ejecta power-index  $n$ . For the  $n = 2$  cases, A2, B2, and E2, the ejecta core is absent, as expected for  $n < 3$ . For the  $n = 4$  cases, A4, B4, and E4, the shocked ejecta contribution is absent because the corresponding electron density vanishes for this density index. The DM components show similar evolutionary behavior among the  $n = 2$  cases, and also among the  $n = 4$  cases. In A2, B2, and E2, the unshocked ejecta dominates the local DM at early times, whereas the contributions from the shocked ejecta and the shocked ambient medium remain negligible throughout the evolution. At later times, the host-galaxy contribution becomes dominant in B2 and E2. By contrast, in A2, where  $DM_{\text{host}}$  is only several tens of  $\text{pc cm}^{-3}$ , the intervening IGM and the Milky Way make important contributions to the total observed DM budget. In A4, B4, and E4, both the unshocked core and the unshocked ejecta make significant contributions to the local DM, while the shocked ambient medium remains not important. In addition, the host-galaxy DM contributions in these three cases are all of order  $10 \text{ pc cm}^{-3}$ . It is worth noting that, even for a low ionization fraction of  $\eta \sim 0.03$ , the two unshocked regions still provide major contributions to the local DM in all six cases and dominate the early-time local DM. This result is consistent with the simulations of Zhang et al. (2026).

The vertical dash-dotted black lines in Figure 2 indicate the transition times from the ED phase to the ST phase, which are derived from the best-fit values of  $M_{\text{ej}}$ ,  $E_k$ , and  $\dot{M}_w$ , together with the fixed wind velocity  $v_w = 100 \text{ km s}^{-1}$ . The inferred transition times for Cases A2, B2, B4, and E2 are on the order of  $10^3$ – $10^4 \text{ yr}$ , whereas those for Cases A4 and E4 are only several hundred years. Observationally, the transition from the ED phase to the ST phase is generally expected to occur on timescales of hundreds to thousands of years (Vink 2020). A relevant example is the Crab Nebula, which is still broadly in a pre-Sedov, ejecta-dominated evolutionary state nearly one millennium after SN 1054. (Trimble 1968). Therefore, the transition times inferred for all the cases are not excluded by the expected evolutionary timescale of young SNRs. Nevertheless, although all the cases correspond to young systems with  $t_0 \lesssim 170 \text{ yr}$ , they imply very different evolutionary stages relative to the ED–ST transition. In particular, A4 has already reached about half of its inferred ED lifetime, and E4 has completed about one fifth of its inferred ED lifetime. By contrast, A2, B2, B4, and E2 are still at less than about 2% of their inferred ED lifetimes, indicating that these systems are observed at a much earlier stage of the ED phase.

The lower panels of Figure 2 present zoom-in views of the observed DM data and show the residuals between the observations and the best-fit model predictions. To make the residual distributions clearer, the bursts observed on the same day are binned together and averaged. For Cases A2, A4, B4, E2, and E4, the residuals of the binned DMs remain relatively close to zero. By contrast, B2 exhibits the clearest systematic drift from positive residuals at earlier epochs to negative residuals at later epochs. This pattern is consistent with its nearly flat DM evolution at burst epoch and indicates that B2 does not reproduce the observed secular DM decrease as well as the other accepted cases.

In Figure 3, we present the best-fits to the observed scattering timescales along with their residuals. It is worth noting that the evolutions of scattering timescales for all cases are significantly similar but with different initial conditions. In particular, B2 and B4 predict much larger scattering timescales at early times than the other cases. This indicates that the retained cases can fit the current data over the observed epoch while still implying very different earlier scattering histories. The lower panels of (a)–(f) show the zoomed-in views of scattering timescales and display the residuals between the observed scattering timescales and the

theoretical predictions. The residuals display a clear systematic upward offset relative to the zero-residual line and are remarkably similar among all six cases. Moreover, the positive residuals are generally more pronounced at later epochs than at earlier ones. This suggests that the observed scattering timescales decrease more slowly with time than predicted by the smooth best-fit curves. Therefore, although the single SNR model reproduces the overall scattering timescale, the drifts of residuals may indicate that the environment of FRB 190520B is more complicated than a one-zone SNR. It may even have small-scale turbulence structures.

To quantify the goodness of fit and compare the retained cases, we evaluate the Bayesian Information Criterion (BIC) and perform a quantile–quantile (Q–Q) analysis of the residuals. Figure 4 presents the Q–Q plots for Cases A2, A4, B2, B4, E2, and E4 in Panels (a)–(f), respectively. These plots compare the empirical quantiles of the normalized residuals with the theoretical quantiles of a norm distributions. Based on these Q–Q plots and the associated coefficients of determination, we characterize the residuals as follows. For the scattering residuals, all six cases give the same coefficient of determination,  $R_{\text{scatter}}^2 = 0.66$ . The scattering residuals deviate systematically from a normal distribution, showing that the adopted SNR model does not fully describe the stochastic or structured variations in the scattering data. For the binned DM residuals, the Q–Q behavior is closer to normal, with  $R_{\text{DM}}^2 = 0.93\text{--}0.95$ . Case B2 gives the largest value,  $R_{\text{DM}}^2 = 0.95$ , but this does not imply the best DM fit, because its residual shifts and BIC value are much larger than those of the statistically preferred cases.

The BIC and  $\Delta\text{BIC}$  values for scattering timescales and observed DMs are summarized in Table 2. For the scattering-timescale data, A2, A4, and E4 give the minimum value,  $\text{BIC}_{\text{scatter}} = 191$ . Case E2 is nearly indistinguishable from them, with  $\Delta\text{BIC}_{\text{scatter}} = 1$ , while B2 and B4 are mildly disfavored, with  $\Delta\text{BIC}_{\text{scatter}} = 5$  and 6, respectively. Therefore, the scattering data alone do not provide a decisive preference among A2, A4, E2, and E4. The DM data provide a much stronger statistical discrimination because of their small observational uncertainties. The minimum value is obtained for E2, with  $\text{BIC}_{\text{DM}} = 1569492$ . For Cases A4, B4, A2, and E4, we have  $\Delta\text{BIC}_{\text{DM}} = 68760, 78996, 102588, \text{ and } 133151$ , respectively. Case B2 is strongly disfavored, with  $\Delta\text{BIC}_{\text{DM}} = 4919321$ , reflecting its inability to reproduce the observed secular DM decrease. Since the DM BIC dominates the statistical comparison, E2 is the statistically favored case among the six solutions.

## 6. DISCUSSIONS

### 6.1. Self-consistency of the scattering theory

The formulae for temporal broadening adopted in Section 3 rely on three standard assumptions that are usually satisfied in ISM-like environments (Rickett 1977): (i) the deviations of the refractive index are much smaller than unity everywhere; (ii) the inner scale  $l_0$  is much larger than the wavelength of the electromagnetic wave,  $\lambda$ ; and (iii) the outer scale  $L$  is much smaller than the thickness of the scattering medium,  $\Delta R$ . In this subsection, we examine whether these assumptions are satisfied in the shocked ejecta and the shocked ambient medium of the SNR, which are the two regions responsible for temporal broadening in our work. This provides a self-consistency check for the parameters favored by the fits.

The deviation of the refractive index induced by electron-density fluctuations is  $\delta n_r = -r_e \lambda^2 \delta n_e / 2\pi$ . For observing frequency of  $\nu = 1.25$  GHz, corresponding to a wavelength of  $\lambda = 24$  cm, the condition  $\delta n_r \ll 1$  is equivalent to  $\delta n_e \ll 3.9 \times 10^{10} \text{ cm}^{-3}$ . Here we use the radial maximum of  $\delta n_e$  at each time as a conservative diagnostic. Figure 5 shows the evolution of this maximum value up to the transition time for Cases A2, A4, B2, B4, E2, and E4. Panels (a) and (b) correspond to the shocked ejecta and the shocked ambient medium, respectively. Only cases with  $n = 2$  appear in the shocked ejecta panel, because the electron density of the shocked ejecta vanishes for  $n = 4$ . In both regions, the maximum values of  $\delta n_e$  remain below  $10^6 \text{ cm}^{-3}$ , which is more than four orders of magnitude smaller than the threshold implied by  $\delta n_r \ll 1$ . Therefore, the small-refractive-index-perturbation condition is safely satisfied in all the six cases.

The second assumption requires  $l_0 \gg \lambda$ . For  $\lambda = 24$  cm, this corresponds to  $l_0 \gg 7.8 \times 10^{-18}$  pc. In addition, for an irregularity spectrum in the inertial range, one also requires  $l_0 \ll L$  (Xu & Zhang 2016). The required scale hierarchy is therefore  $\lambda \ll l_0 \ll L$ . Figure 6 shows the time evolution of the radial maximum of  $l_0$  in the shocked ejecta and the shocked ambient medium, corresponding to Panels (a) and (b), respectively. The evolution of  $L/10$  and the horizontal line representing  $10\lambda$  are also shown in Figure 6. Thus, the separations between  $l_0$ ,  $10\lambda$ , and  $L/10$  are visualized directly. Because  $l_0$  is estimated as

described in Section 3 and is related to  $n_e$ , only cases with  $n = 2$  have non-zero values of  $l_0$  in the shocked ejecta. Figure 6 shows that, throughout the ED phase, the maximum value of  $l_0$  stays below  $0.1L$  and above  $10\lambda$  in all cases. This indicates that the condition  $\lambda \ll l_0 \ll L$  is satisfied with a clear margin. The treatment of the inner scale  $l_0$  remains one of the main sources of uncertainty in the scattering calculation. In the ISM,  $l_0$  is usually constrained by observations. For example, [Armstrong et al. \(1995\)](#) used observational data from nearby pulsars within  $\sim 1$  kpc to derive an upper limit on the ISM inner scale of  $\sim 10^{-8}$  pc, while [Gupta et al. \(1993\)](#) inferred a range of  $l_0 \sim 10^{-9}$ – $10^{-7}$  pc from pulsar observations.

Figures 7(a) and (b) show the evolution of the thickness  $\Delta R$  in the shocked ejecta and the shocked ambient medium, respectively, while Figures 7(c) and (d) show the corresponding evolution of  $\Delta R/L$  in these two regions. It can be seen that  $\Delta R/L$  is always larger than 10 in all retained cases, which means that the outer scale remains sufficiently smaller than the thickness of the scattering layer throughout the relevant evolutionary stage. A noteworthy feature is that, although  $\Delta R$  itself increases monotonically with time, the ratio  $\Delta R/L$  generally decreases. This indicates that the outer scale grows faster than the shell thickness during the ED phase. This trend is physically reasonable, because in the ST phase the outer scale is usually expected to become comparable to the thickness of the shocked regions ([Chevalier 1982](#); [Dwarkadas 2000](#)). Therefore, the three assumptions underlying the scattering formulae are all satisfied with substantial margins. Overall, these checks show that the six retained cases lie in a regime where the adopted scattering theory is self-consistent.

## 6.2. Free-free absorption

Another important issue is whether the surrounding SNR is transparent to the radio bursts from FRB 190520B. Radio waves may experience free-free absorption in SNR. The absorption coefficient is ([Rybicki & Lightman 1979](#))

$$\alpha_\nu^{\text{ff}} = 0.018 T^{-3/2} Z^2 n_e n_i \nu^{-2} \bar{g}_{\text{ff}}, \quad (44)$$

where  $T$  is the plasma temperature,  $Z$  is the ionic charge number,  $n_i$  is the ion density,  $\nu$  is the frequency of radio emission, and  $\bar{g}_{\text{ff}}$  is the Gaunt factor. In our calculation, we approximate the free-free optical depth as

$$\tau_{\text{ff}} \approx \alpha_\nu^{\text{ff}} \Delta R. \quad (45)$$

We adopt  $Z \sim 1$ ,  $n_i \sim n_e$ , and  $\bar{g}_{\text{ff}} \sim 1$ . For FRB 190520B, the frequency of bursts is set to  $\nu = 1.25$  GHz. The temperatures in the two unshocked regions are set to  $10^4$  K ([Metzger et al. 2017](#); [Zhao et al. 2021](#)). For the shocked regions, we use the downstream proton temperature,  $T_p$ , as an approximation for the plasma temperature, where

$$k_B T_p = \frac{3}{16} m_p V_s^2, \quad (46)$$

where  $k_B$  is the Boltzmann constant. The reverse- and forward-shock velocities are obtained by differentiating Equations (10) and (12) with respect to time.

Figure 8 shows the time evolution of  $\tau_{\text{ff}}$  for all six cases. It can be seen that the optical depth decreases rapidly with time and drops below unity from several decades to about one century for all cases. Among the six cases, B4 remains optically thick for the longest time, becoming transparent at  $t \simeq 114$  yr. Cases A4 and E4, with transparency times of  $t \simeq 100$  and 111 yr, respectively, also remain opaque longer than A2, B2, and E2, whose transparency times are  $t \simeq 80$ , 21, and 43 yr, respectively. Nevertheless, in all six cases the SNR becomes transparent to 1.25 GHz bursts before the inferred source age of FRB 190520B. This means that the surrounding remnant is unlikely to prevent the escape of the observed GHz radio bursts.

This result can also be understood together with Figure 7. Although the shell thickness  $\Delta R$  increases monotonically with time,  $\tau_{\text{ff}}$  decreases by many orders of magnitude. Therefore, it can be concluded that the time evolution of the free-free opacity is controlled primarily by the rapid decline of the density, rather than by the increase in the propagation length. Finally, Equation (43) shows that  $\tau_{\text{ff}} \propto \nu^{-2}$  for fixed plasma properties. The transparency condition is therefore frequency dependent: even if the local SNR is already transparent at GHz, it can remain opaque for a longer period at lower radio frequencies. Hence, within

the SNR scenarios, a young local environment can still be compatible with the detection of GHz bursts from FRB 190520B, while displaying a suppression of lower frequency emission. Together with the evolutions of DMs and scattering timescales, we conclude that the six cases point out to a physically plausible evolutionary stage of the SNR: it is still young enough to provide appreciable local DM and scattering timescales, but already evolved enough to become transparent for GHz radio emissions.

### 6.3. Physical implications

It is worth noting that the present framework reproduces the secular DM evolution more successfully than the detailed evolution of the scattering timescale. As shown in Section 5, the DM residuals are closer to a normal distribution, indicating that the local DM evolution of FRB 190520B can be described well by a single expanding SNR. The scattering residuals, however, show a systematic positive offset, especially at later epochs. This suggests that the observed scattering timescales are larger than those predicted by the adopted scattering theory, or equivalently that the observed scattering decreases more slowly than the model expectation. A natural possibility is that an additional scattering component is present along the line of sight. Indeed, [Ocker et al. \(2023\)](#) reported scattering variations of FRB 190520B on timescales from minutes to days, which are not clearly correlated with the observed DMs and were attributed to a dynamic and inhomogeneous circumsource medium. Alternatively, the systematic upward drift of the scattering residuals may indicate that some bursts pass through more turbulent or clumpy regions in the SNR, where enhanced density fluctuations produce stronger temporal broadening. Therefore, while the SNR model can capture the secular evolution of the DM, the scattering data likely require an extra component associated with the central engine, or additional small-scale turbulent structures.

The inferred source ages,  $t_0 = 79.8\text{--}169.8$  yr, indicate that the central engine is very young. This age range is compatible with the scenario in which an active newborn magnetar is embedded in an expanding SNR. In our work,  $DM_{\text{host}}$  represents a time-independent host contribution and provides information on the host environment of FRB 190520B. Cases A2, A4, B4, and E4 predict extremely small values of  $DM_{\text{host}}$ , of the order of several tens of  $\text{pc cm}^{-3}$ . In these cases, the observed secular DM evolution is mainly driven by the expanding local environment, especially the young SNR. Such low host contributions, besides, indicate either the source of FRB 190520B is located an offset region of the host galaxy, or it is embedded in a bubble cavity. Since FRB 190520B is located at a star-forming region in its host, if such low  $DM_{\text{host}}$  is real, the former scenario is more possible. Case B2 is the opposite one, requiring the largest host contribution,  $DM_{\text{host}} \simeq 10^3 \text{ pc cm}^{-3}$ . As a result, the predicted DM at burst epoch becomes almost flat, with a slope of only  $-0.3 \text{ pc cm}^{-3} \text{ yr}^{-1}$ . This is in clear tension with the observed secular DM decrease of FRB 190520B. Case E2 provides an intermediate scenario. It has  $DM_{\text{host}} \simeq 400 \text{ pc cm}^{-3}$ , implying that both the host-galaxy component and the local SNR component make important contributions to the total observed DM. Physically, this case corresponds to a young SNR embedded in a relatively high-density host environment, such as a dense star-forming region, or an HII-region. This case is then broadly consistent with the fact that FRB 190520B is located in an active star-forming environment and is associated with a compact PRS ([Niu et al. 2022](#)). Future monitoring of the DM evolution can help break this degeneracy between the host and the local contribution: if the observed DM approaches a high floor, a large  $DM_{\text{host}}$  component would be favored; if it continues to decline steadily, the low- $DM_{\text{host}}$ , local-dominated solutions would become more plausible.

All the six cases require relatively large ejecta masses,  $M_{\text{ej}} = 8.7\text{--}19.2 M_{\odot}$ . However, the inferred kinetic energies and wind mass-loss rates span broad ranges, with  $E_{\text{k}} = 0.1\text{--}7.3 \times 10^{51} \text{ erg}$  and  $\dot{M}_{\text{w}} = 0.3\text{--}14.8 \times 10^{-5} M_{\odot} \text{ yr}^{-1}$  for the adopted wind velocity  $v_{\text{w}} = 100 \text{ km s}^{-1}$ . Therefore, the present fits do not uniquely determine either the explosion energy or the progenitor mass-loss preference. Thus, while a massive-star progenitor is favored, the current fitting results alone are insufficient to identify a unique supernova subtype. The conservative picture is that FRB 190520B is associated with a young, massive-star core-collapse SNR expanding into a moderately dense progenitor wind.

It is also noteworthy that the two Kolmogorov-spectrum prescriptions fail to reproduce the observations. This fact, however, does not indicate the non-existence of Kolmogorov-spectrum turbulence in SNRs. Observational evidence for Kolmogorov-like turbulence has been reported in many SNRs. For example, [Shimoda et al. \(2018\)](#) found a Kolmogorov-like magnetic energy spectrum in Tycho's SNR. The failure of the Kolmogorov-spectrum prescriptions here is more likely related to their specific

implementation in the scattering model. In our calculation, the outer scale  $L$  is estimated from a linear fit to the simulation results of Dwarkadas (2000). With this prescription,  $L$  grows too rapidly for the theoretical scattering timescales to fit the observational data. If the outer scale instead followed a time-dependent relation with a much smaller growth rate, while still remaining much larger than the inner scale, the Kolmogorov-spectrum prescriptions may reproduce the observations.

Overall, combining the statistical results with the physical interpretation, E2 is the most favored case in the present framework. It gives the minimum  $\text{BIC}_{\text{DM}}$ , predicts a DM slope that lies within the range given by Niu et al. (2026), and remains competitive in the scattering fit. Physically, its fitted SNR parameters,  $M_{\text{ej}}$ ,  $E_{\text{k}}$ , and  $\dot{M}_{\text{w}}$ , are all reasonable. In particular, the partition between the local and host DM contributions in this case is more reasonable than in the other cases. Although its transition time is somewhat long, it is still acceptable.

## 7. SUMMARY

In this work, we test the scenario that FRB 190520B originates from a central engine formed in the core-collapse of a massive star and embedded in a SNR expanding into a wind environment. The SNR evolution is described by the self-similar solution, with an ejecta-envelope density index of  $n = 2, 4, 6, \text{ or } 8$ . We combine the self-similar SNR model with five prescriptions for temporal broadening induced by plasma density irregularities, and use the observed DM and scattering-timescale data of FRB 190520B to constrain the properties of its local environment. Our main conclusions are summarized as below:

- (i) Among the 20 cases explored in this work, only six cases are retained by the fitting procedure, namely A2, A4, B2, B4, E2, and E4. All retained cases correspond to the FE solution with  $n = 2$  or 4, while none of the SSDW cases with  $n = 6$  or 8 can reproduce the observational data. The two Kolmogorov-type turbulence spectra are also inconsistent with the data, which may result from the adopted implementation of an overly large outer scale  $L$ .
- (ii) All retained cases imply a very young SNR for FRB 190520B, with source ages of  $t_0 = 79.8\text{--}169.8$  yr. The inferred ejecta masses are relatively large,  $M_{\text{ej}} = 8.7\text{--}19.2 M_{\odot}$ , favoring a massive-star core-collapse origin. However, the inferred kinetic energies and wind mass-loss rates span broad ranges, with  $E_{\text{k}} = 0.1\text{--}7.3 \times 10^{51}$  erg and  $\dot{M}_{\text{w}} = 0.3\text{--}14.8 \times 10^{-5} M_{\odot} \text{ yr}^{-1}$  for the adopted wind velocity  $v_{\text{w}} = 100 \text{ km s}^{-1}$ . Hence, the current modeling is insufficient to identify a unique supernova subtype.
- (iii) The fitted values of  $DM_{\text{host}}$  imply different physical pictures for the host and its local contributions. Cases A2, A4, B4, and E4 require a relatively small  $DM_{\text{host}}$  value, indicating that the observed DM evolution is dominated mainly by the local SNR contribution. B2 represents the opposite extreme, with  $DM_{\text{host}} \simeq 10^3 \text{ pc cm}^{-3}$ , and is strongly disfavored because it predicts an almost flat DM evolution during the burst epoch. E2 provides an intermediate and more plausible scenario, in which both the host-galaxy component and the local SNR component are important contributors to the total observed DM.
- (iv) The secular DM evolution is reproduced more successfully than the detailed evolution of the scattering timescale. Except for B2, the retained cases predict DM slopes broadly consistent with the observed long-term DM decrease. By contrast, the scattering residuals show a systematic upward drift. This suggests that an additional scattering component or more turbulent structures in the SNR may be present.
- (v) We also examined the self-consistency of the scattering theory. For the retained cases, the assumptions underlying the temporal-broadening formalism are satisfied within the relevant parameter ranges. In addition, the optical depth of free-free absorption at 1.25 GHz drops below unity before the inferred source ages in all retained cases. Therefore, the local SNR can remain young enough to provide appreciable DM and scattering, while already being transparent to the observed GHz bursts from the central engine.
- (vi) Combining the statistical results with the physical interpretation, E2 is the most favored case in the SNR framework.

## ACKNOWLEDGEMENTS

We are grateful to Zhen-Yi Zhao for his helpful suggestions. This study is supported by the National Natural Science Foundation of China (Grant Nos. 12233002, 12273113), and by the National Key R&D Program of China (2021YFA0718500). YFH acknowledges the support from the Xinjiang Tianchi Program. Jin-Jun Geng acknowledges support from the Youth Innovation Promotion Association (2023331)

## REFERENCES

- Anna-Thomas, R., Connor, L., Dai, S., et al. 2023, *Science*, 380, 599, doi: [10.1126/science.abo6526](https://doi.org/10.1126/science.abo6526)
- Armstrong, J. W., Rickett, B. J., & Spangler, S. R. 1995, *ApJ*, 443, 209, doi: [10.1086/175515](https://doi.org/10.1086/175515)
- Beloborodov, A. M. 2020, *ApJ*, 896, 142, doi: [10.3847/1538-4357/ab83eb](https://doi.org/10.3847/1538-4357/ab83eb)
- Bhattacharya, M., Murase, K., & Kashiyama, K. 2025, *MNRAS*, doi: [10.1093/mnras/staf2175](https://doi.org/10.1093/mnras/staf2175)
- Bochenek, C. D., Ravi, V., Belov, K. V., et al. 2020, *Nature*, 587, 59, doi: [10.1038/s41586-020-2872-x](https://doi.org/10.1038/s41586-020-2872-x)
- Chatterjee, S., Law, C. J., Wharton, R. S., et al. 2017, *Nature*, 541, 58, doi: [10.1038/nature20797](https://doi.org/10.1038/nature20797)
- Chevalier, R. A. 1982, *ApJ*, 258, 790, doi: [10.1086/160126](https://doi.org/10.1086/160126)
- Chevalier, R. A., & Fransson, C. 2017, in *Handbook of Supernovae*, ed. A. W. Alsabti & P. Murdin, 875, doi: [10.1007/978-3-319-21846-5\\_34](https://doi.org/10.1007/978-3-319-21846-5_34)
- CHIME/FRB Collaboration, Andersen, B. C., Bandura, K. M., et al. 2020, *Nature*, 587, 54, doi: [10.1038/s41586-020-2863-y](https://doi.org/10.1038/s41586-020-2863-y)
- CHIME/FRB Collaboration, Abbott, T., Andersen, B. C., et al. 2026, arXiv e-prints, arXiv:2601.09399, doi: [10.48550/arXiv.2601.09399](https://doi.org/10.48550/arXiv.2601.09399)
- Coles, W. A., & Harmon, J. K. 1989, *ApJ*, 337, 1023, doi: [10.1086/167173](https://doi.org/10.1086/167173)
- Cordes, J. M., & Lazio, T. J. W. 2002, arXiv e-prints, astro, doi: [10.48550/arXiv.astro-ph/0207156](https://doi.org/10.48550/arXiv.astro-ph/0207156)
- Dai, Z. G., Wang, J. S., Wu, X. F., & Huang, Y. F. 2016, *ApJ*, 829, 27, doi: [10.3847/0004-637X/829/1/27](https://doi.org/10.3847/0004-637X/829/1/27)
- Dwarkadas, V. V. 2000, *ApJ*, 541, 418, doi: [10.1086/309406](https://doi.org/10.1086/309406)
- Fraschetti, F., Teyssier, R., Ballet, J., & Decourchelle, A. 2010, *A&A*, 515, A104, doi: [10.1051/0004-6361/200912692](https://doi.org/10.1051/0004-6361/200912692)
- Geng, J. J., & Huang, Y. F. 2015, *ApJ*, 809, 24, doi: [10.1088/0004-637X/809/1/24](https://doi.org/10.1088/0004-637X/809/1/24)
- Giacomazzo, B., & Perna, R. 2013, *ApJL*, 771, L26, doi: [10.1088/2041-8205/771/2/L26](https://doi.org/10.1088/2041-8205/771/2/L26)
- Gupta, Y., Rickett, B. J., & Coles, W. A. 1993, *ApJ*, 403, 183, doi: [10.1086/172193](https://doi.org/10.1086/172193)
- Hwang, U., & Laming, J. M. 2012, *ApJ*, 746, 130, doi: [10.1088/0004-637X/746/2/130](https://doi.org/10.1088/0004-637X/746/2/130)
- Katz, J. I. 2016, *ApJ*, 818, 19, doi: [10.3847/0004-637X/818/1/19](https://doi.org/10.3847/0004-637X/818/1/19)
- Laming, J. M., & Hwang, U. 2003, *ApJ*, 597, 347, doi: [10.1086/378268](https://doi.org/10.1086/378268)
- Lee, L. C., & Jokipii, J. R. 1975a, *ApJ*, 201, 532, doi: [10.1086/153916](https://doi.org/10.1086/153916)
- . 1975b, *ApJ*, 196, 695, doi: [10.1086/153458](https://doi.org/10.1086/153458)
- Li, D., Wang, P., Zhu, W. W., et al. 2021, *Nature*, 598, 267, doi: [10.1038/s41586-021-03878-5](https://doi.org/10.1038/s41586-021-03878-5)
- Lorimer, D. R., Bailes, M., McLaughlin, M. A., Narkevic, D. J., & Crawford, F. 2007, *Science*, 318, 777, doi: [10.1126/science.1147532](https://doi.org/10.1126/science.1147532)
- Luan, J., & Goldreich, P. 2014, *ApJL*, 785, L26, doi: [10.1088/2041-8205/785/2/L26](https://doi.org/10.1088/2041-8205/785/2/L26)
- Lyubarsky, Y. 2020, *ApJ*, 897, 1, doi: [10.3847/1538-4357/ab97b5](https://doi.org/10.3847/1538-4357/ab97b5)
- Metzger, B. D., Berger, E., & Margalit, B. 2017, *ApJ*, 841, 14, doi: [10.3847/1538-4357/aa633d](https://doi.org/10.3847/1538-4357/aa633d)
- Micelotta, E. R., Dwek, E., & Slavin, J. D. 2016, *A&A*, 590, A65, doi: [10.1051/0004-6361/201527350](https://doi.org/10.1051/0004-6361/201527350)
- Nadezhin, D. K. 1985, *Ap&SS*, 112, 225, doi: [10.1007/BF00653506](https://doi.org/10.1007/BF00653506)
- Niu, C. H., Aggarwal, K., Li, D., et al. 2022, *Nature*, 606, 873, doi: [10.1038/s41586-022-04755-5](https://doi.org/10.1038/s41586-022-04755-5)
- Niu, C.-H., Li, D., Yang, Y.-P., et al. 2026, *Science Bulletin*, 71, 76, doi: [10.1016/j.scib.2025.11.023](https://doi.org/10.1016/j.scib.2025.11.023)
- Ocker, S. K., Cordes, J. M., Chatterjee, S., et al. 2023, *MNRAS*, 519, 821, doi: [10.1093/mnras/stac3547](https://doi.org/10.1093/mnras/stac3547)
- Rahaman, S. M., Acharya, S. K., Beniamini, P., & Granot, J. 2025, *ApJ*, 988, 276, doi: [10.3847/1538-4357/ade70c](https://doi.org/10.3847/1538-4357/ade70c)
- Ricci, R., Piro, L., Panessa, F., et al. 2021, *The Astronomer's Telegram*, 14549, 1
- Rickett, B. J. 1977, *Annual Review of Astronomy and Astrophysics*, 15, 479, doi: [10.1146/annurev.aa.15.090177.002403](https://doi.org/10.1146/annurev.aa.15.090177.002403)
- Rickett, B. J. 1990, *ARA&A*, 28, 561, doi: [10.1146/annurev.aa.28.090190.003021](https://doi.org/10.1146/annurev.aa.28.090190.003021)
- Rybicki, G. B., & Lightman, A. P. 1979, *Radiative processes in astrophysics*
- Shimoda, J., Akahori, T., Lazarian, A., Inoue, T., & Fujita, Y. 2018, *MNRAS*, 480, 2200, doi: [10.1093/mnras/sty2034](https://doi.org/10.1093/mnras/sty2034)
- Shirkey, R. C. 1978, *ApJ*, 224, 477, doi: [10.1086/156395](https://doi.org/10.1086/156395)
- Smartt, S. J. 2009, *ARA&A*, 47, 63, doi: [10.1146/annurev-astro-082708-101737](https://doi.org/10.1146/annurev-astro-082708-101737)
- Smith, N. 2014, *ARA&A*, 52, 487, doi: [10.1146/annurev-astro-081913-040025](https://doi.org/10.1146/annurev-astro-081913-040025)

- Spitler, L. G., Cordes, J. M., Hessels, J. W. T., et al. 2014, *ApJ*, 790, 101, doi: [10.1088/0004-637X/790/2/101](https://doi.org/10.1088/0004-637X/790/2/101)
- Spitler, L. G., Scholz, P., Hessels, J. W. T., et al. 2016, *Nature*, 531, 202, doi: [10.1038/nature17168](https://doi.org/10.1038/nature17168)
- Tang, X., & Chevalier, R. A. 2017, *MNRAS*, 465, 3793, doi: [10.1093/mnras/stw2978](https://doi.org/10.1093/mnras/stw2978)
- Tendulkar, S. P., Bassa, C. G., Cordes, J. M., et al. 2017, *ApJL*, 834, L7, doi: [10.3847/2041-8213/834/2/L7](https://doi.org/10.3847/2041-8213/834/2/L7)
- Thornton, D., Stappers, B., Bailes, M., et al. 2013, *Science*, 341, 53, doi: [10.1126/science.1236789](https://doi.org/10.1126/science.1236789)
- Trimble, V. 1968, *AJ*, 73, 535, doi: [10.1086/110658](https://doi.org/10.1086/110658)
- Truelove, J. K., & McKee, C. F. 1999, *ApJS*, 120, 299, doi: [10.1086/313176](https://doi.org/10.1086/313176)
- Vink, J. 2020, *Physics and Evolution of Supernova Remnants*, doi: [10.1007/978-3-030-55231-2](https://doi.org/10.1007/978-3-030-55231-2)
- Wang, F. Y., Lan, H. T., Zhao, Z. Y., et al. 2025, arXiv e-prints, arXiv:2512.07140. <https://arxiv.org/abs/2512.07140>
- Wei, J.-P., Huang, Y.-F., Cui, L., et al. 2025, *ApJ*, 980, 114, doi: [10.3847/1538-4357/adace3](https://doi.org/10.3847/1538-4357/adace3)
- Xu, S., & Zhang, B. 2016, *ApJ*, 832, 199, doi: [10.3847/0004-637X/832/2/199](https://doi.org/10.3847/0004-637X/832/2/199)
- Yang, Y.-P., Lu, W., Feng, Y., Zhang, B., & Li, D. 2022, *ApJL*, 928, L16, doi: [10.3847/2041-8213/ac5f46](https://doi.org/10.3847/2041-8213/ac5f46)
- Yoon, S.-C., Podsiadlowski, P., & Rosswog, S. 2007, *MNRAS*, 380, 933, doi: [10.1111/j.1365-2966.2007.12161.x](https://doi.org/10.1111/j.1365-2966.2007.12161.x)
- Zhang, B. 2017, *ApJL*, 836, L32, doi: [10.3847/2041-8213/aa5ded](https://doi.org/10.3847/2041-8213/aa5ded)
- . 2018, *The Physics of Gamma-Ray Bursts* (Cambridge University Press), doi: [10.1017/9781139226530](https://doi.org/10.1017/9781139226530)
- . 2023, *Reviews of Modern Physics*, 95, 035005, doi: [10.1103/RevModPhys.95.035005](https://doi.org/10.1103/RevModPhys.95.035005)
- Zhang, Z. J., Kawashima, G., Lee, S.-H., et al. 2026, arXiv e-prints, arXiv:2603.07012. <https://arxiv.org/abs/2603.07012>
- Zhao, Z. Y., Zhang, G. Q., Wang, Y. Y., Tu, Z.-L., & Wang, F. Y. 2021, *ApJ*, 907, 111, doi: [10.3847/1538-4357/abd321](https://doi.org/10.3847/1538-4357/abd321)
- Zhong, S.-Q., & Dai, Z.-G. 2020, *ApJ*, 893, 9, doi: [10.3847/1538-4357/ab7bdf](https://doi.org/10.3847/1538-4357/ab7bdf)

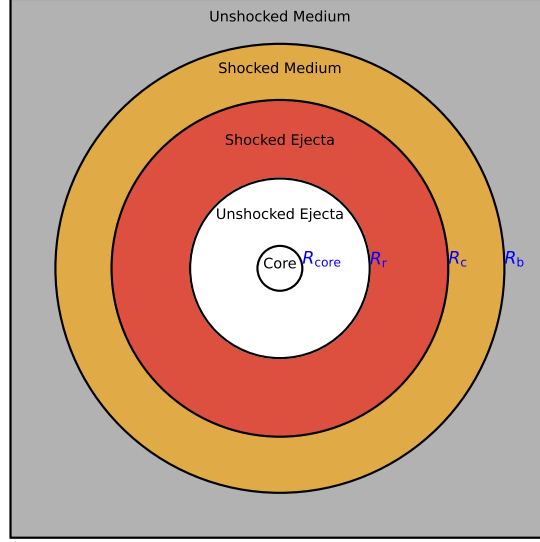


**Figure 1.** Schematic illustration of a SNR in the self-similar solution.

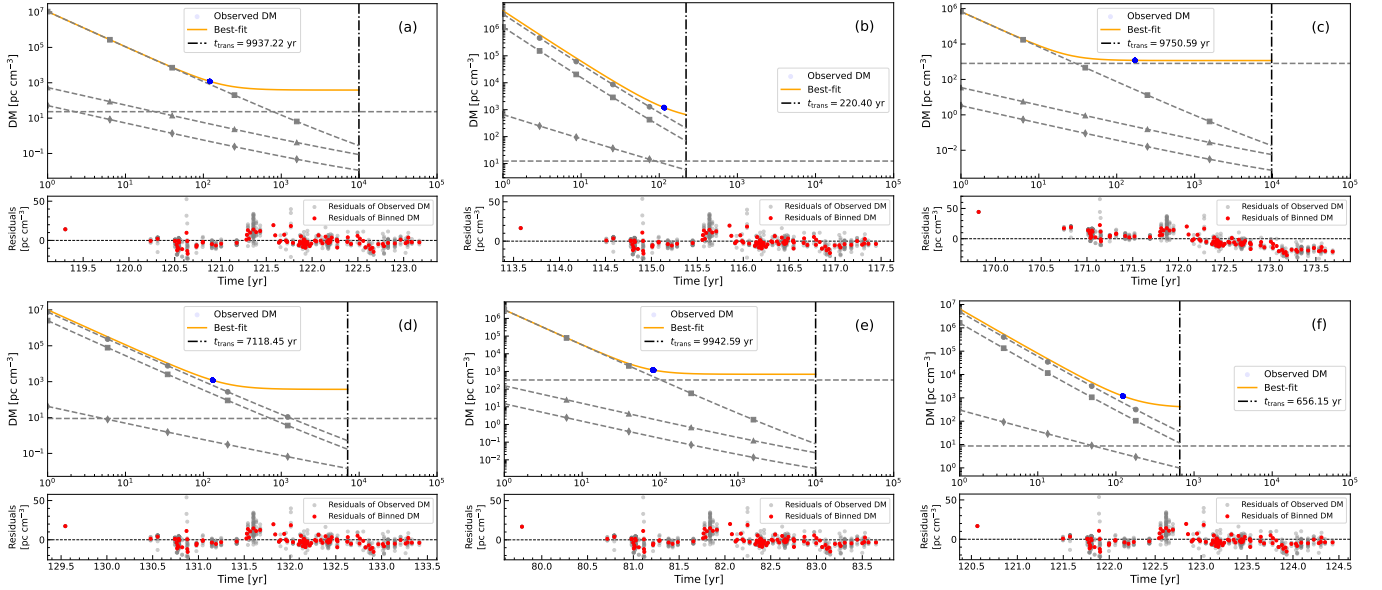


**Figure 2.** Evolution of the DM and the corresponding residuals. Panels (a), (b), (c), (d), (e), and (f) correspond to Cases A2, A4, B2, B4, E2, and E4, respectively. In the upper panels, the orange lines show the best-fit DM evolution, and the grouped blue dots are the observed DM. The horizontal gray dashed lines without markers are  $DM_{\text{host}}$ , while the dashed curves marked by circles, squares, triangles, and diamonds represent the DM contributions from the unshocked core, unshocked ejecta, shocked ejecta, and shocked ambient medium, respectively. The vertical black dash-dotted lines represent the transition times. In the lower panels, the gray and red dots are the residuals of observed DM and binned DM, respectively. The horizontal black dashed lines indicate the zero residual.

## APPENDIX

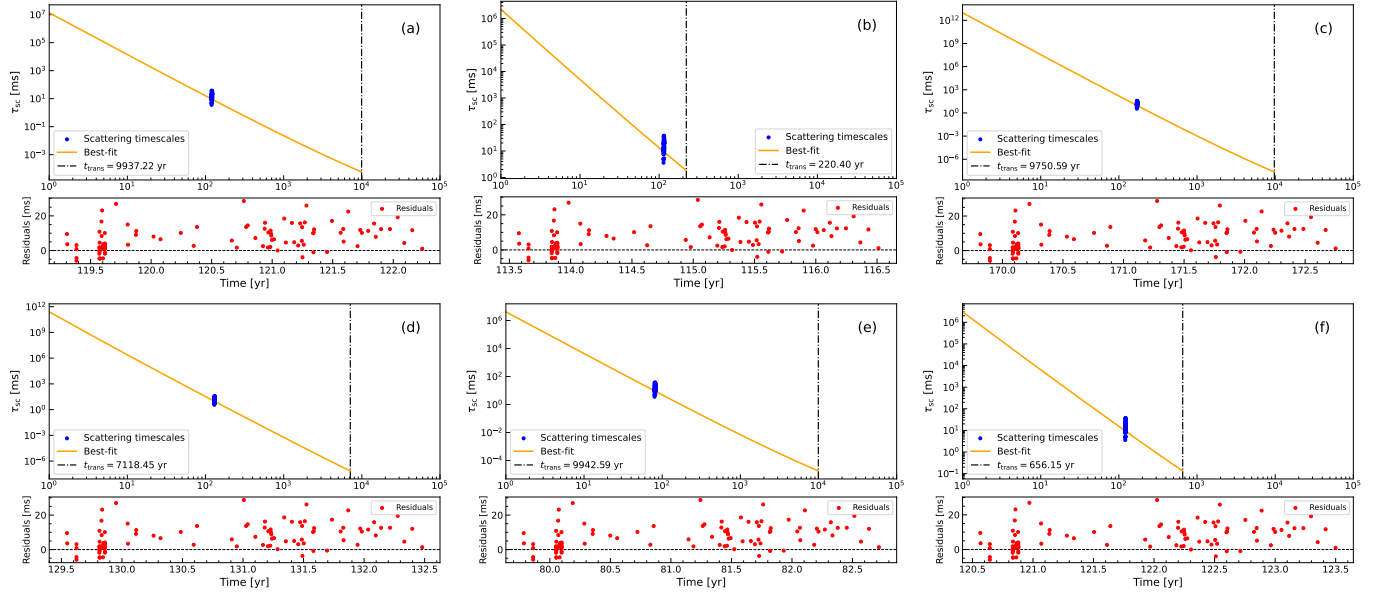


**Figure 3.** Evolution of the scattering timescale and the corresponding residuals. Panels (a), (b), (c), (d), (e), and (f) correspond to Cases A2, A4, B2, B4, E2, and E4, respectively. In the upper panels, the orange lines show the best-fit evolution of the scattering timescale, and the blue dots are the observed scattering timescales. The vertical black dash-dotted lines mark the transition times. In the lower panels, the red dots are the residuals of scattering timescales, and the horizontal black dashed lines are the zero residual.

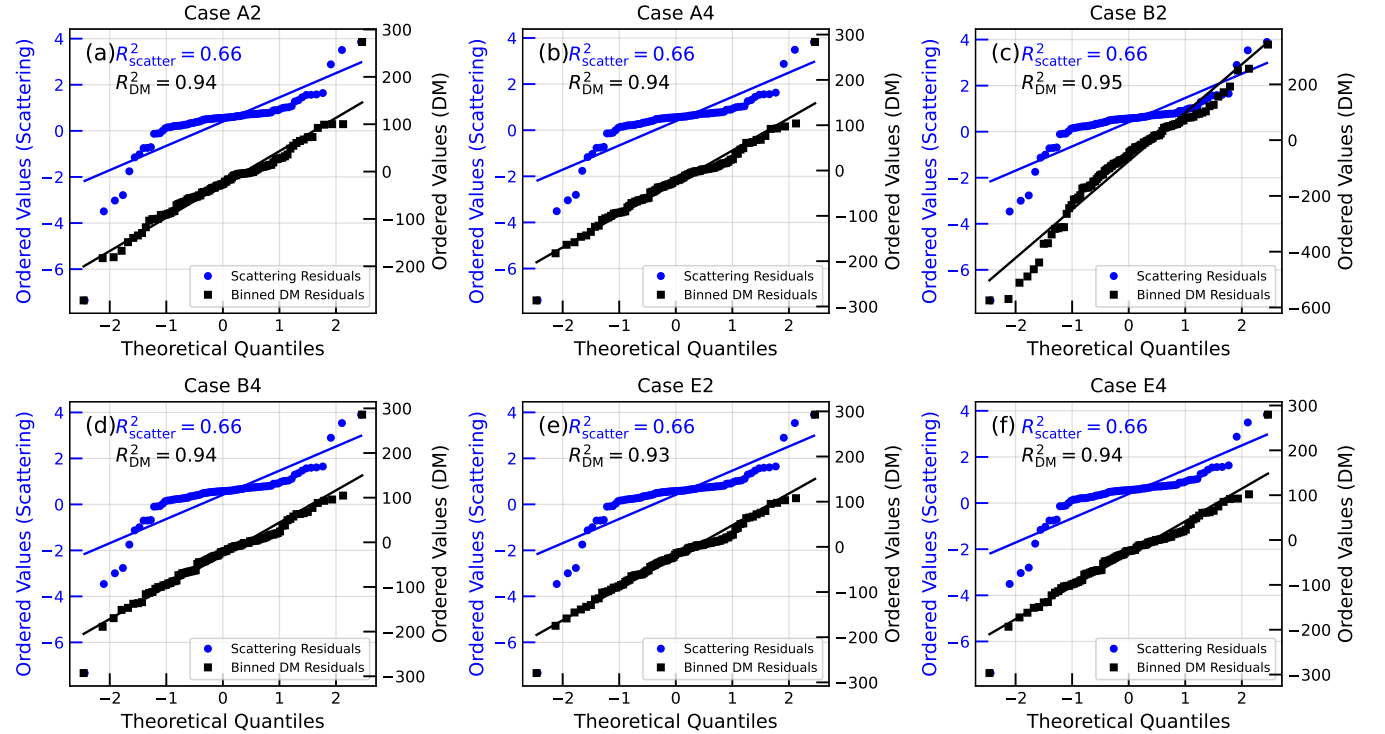


**Figure 4.** The Q-Q plots of the residuals of DM and scattering timescale. Panels (a), (b), (c), (d), (e), and (f) correspond to Cases A2, A4, B2, B4, E2, and E4, respectively. The blue points represent the residuals of the scattering timescales and are referenced to the left y-axis, while the black points represent the residuals of the binned DMs and are referenced to the right y-axis. The blue and black lines are the corresponding linear fits.  $R^2_{scatter}$  and  $R^2_{DM}$  are the determined coefficients of residuals of the observed DM and scattering timescales, respectively.

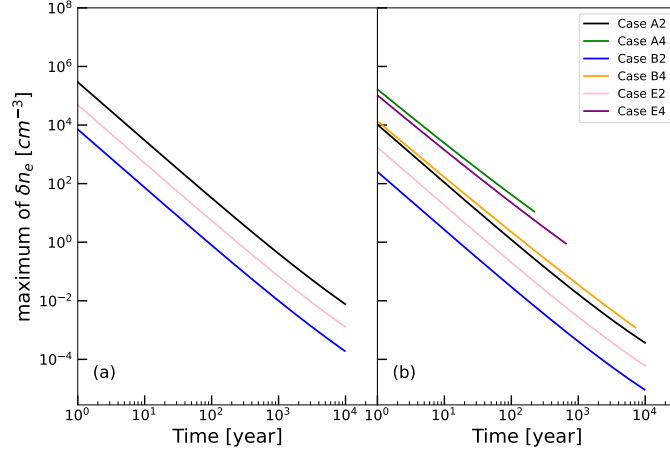


**Figure 5.** Evolution of the maximum density fluctuation along radial direction,  $\delta n_e$ , in the shocked ejecta and shocked ambient medium, shown in Panels (a) and (b), respectively. The black, green, blue, orange, pink, and purple curves correspond to Cases A2, A4, B2, B4, E2, and E4, respectively.

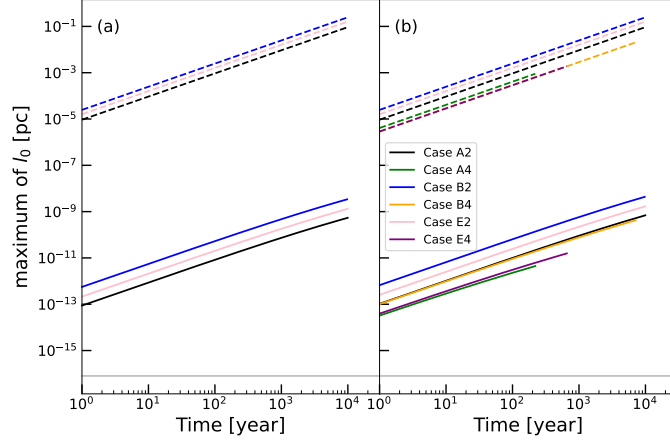


**Figure 6.** Evolution of the maximum inner scale  $l_0$  along the radial direction, in the shocked ejecta and shocked ambient medium, shown in Panels (a) and (b), respectively. The black, green, blue, orange, pink, and purple curves correspond to Cases A2, A4, B2, B4, E2, and E4, respectively. The solid curves show the evolution of the maximum inner scale  $l_0$  along the radial direction, while the dashed curves show the evolution of  $L/10$ , where  $L$  is the outer scale. The horizontal gray lines indicate  $10\lambda$ .

Cases	$M_{ej}/M_{\odot}$	$E_k/10^{51}$ erg	$\dot{M}_w/10^{-5} M_{\odot} \text{ yr}^{-1}$	$t_0/\text{yr}$	$DM_{\text{host}}/\text{pc cm}^{-3}$	$\beta$	$t_{\text{tran}}/\text{yr}$
A2	19.2	2.3	1.9	119.3	28.7	×	9937.2
A4	13.7	0.3	14.8	113.6	15.3	×	220.4
B2	8.7	7.3	0.3	169.8	998.0	2.9	9750.6
B4	17.5	0.2	0.8	129.5	11.0	2.9	7118.5
E2	16.7	6.0	1.0	79.8	407.6	×	9942.6
E4	10.2	0.1	5.2	120.6	10.7	×	656.2

**Table 1.** Best-fit parameters and inferred transition times for Cases A2, A4, B2, B4, E2, and E4.

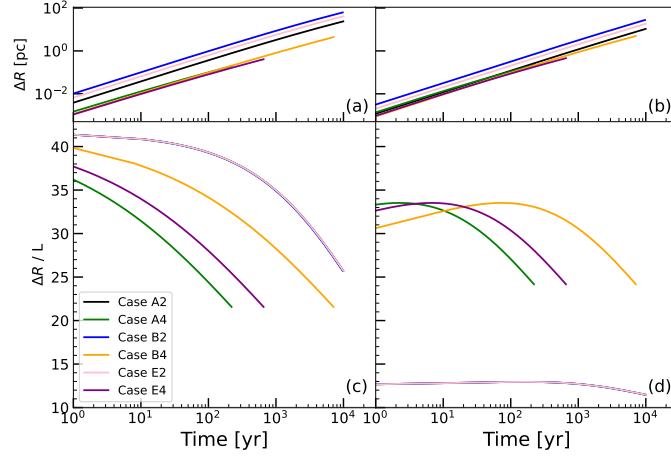


**Figure 7.** Evolution of the plasma thickness in the shocked ejecta and shocked ambient medium, shown in Panels (a) and (b), respectively. Panels (c) and (d) show the corresponding evolution of the ratio between the plasma thickness and the outer scale,  $\Delta R/L$ , in the shocked ejecta and shocked ambient medium. The black, green, blue, orange, pink, and purple curves correspond to Cases A2, A4, B2, B4, E2, and E4, respectively.

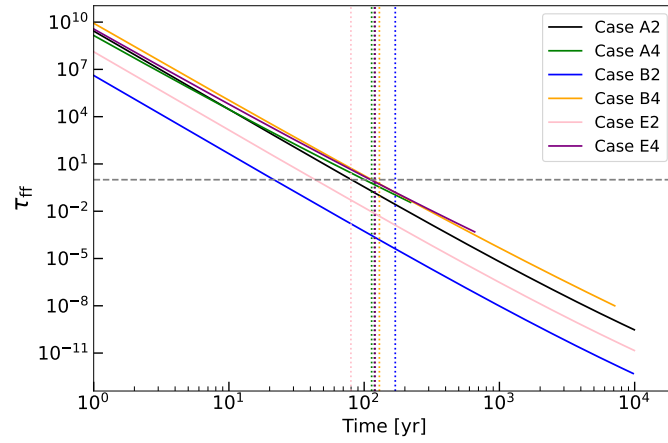


**Figure 8.** Evolution of the free-free optical depth. The black, green, blue, orange, pink, and purple curves correspond to Cases A2, A4, B2, B4, E2, and E4, respectively. The solid curves show the evolution of the optical depth, while the vertical dotted lines mark the inferred source ages. The horizontal gray dashed line indicates  $\tau_{\text{ff}} = 1$ .

Cases	$\text{BIC}_{\text{scatter}}$	$\Delta\text{BIC}_{\text{scatter}}$	$\text{BIC}_{\text{DM}}$	$\Delta\text{BIC}_{\text{DM}}$
A2	191	0	1672080	102588
A4	191	0	1638253	68760
B2	196	5	6488813	4919321
B4	197	6	1648488	78996
E2	192	1	1569492	0
E4	191	0	1702643	133151

**Table 2.** BIC and  $\Delta\text{BIC}$  values for the scattering-timescale and DM fits of Cases A2, A4, B2, B4, E2, and E4.

### A. DERIVATION OF PULSE BROADENING FOR A GAUSSIAN DENSITY FLUCTUATION SPECTRUM

Following [Rickett \(1977\)](#), the density fluctuation of a Gaussian spectrum is

$$P_{3N}(k) = C_N^2 \exp[-k^2/k_0^2], \quad (\text{A1})$$

where  $k_0 = 2\pi/l_0$ . Since the normalization of the Gaussian spectrum is performed over the entire wavenumber space, we obtain

$$C_N^2 = \delta n_e^2 / k_0^3 \pi^{3/2}. \quad (\text{A2})$$

According to Equation A7 in [Rickett \(1990\)](#), the wave structure function can be written as

$$D_\phi = 4\pi r_e^2 \lambda^2 C_N^2 \Delta D \int_0^{2\pi} \int_0^\infty [1 - \cos(\vec{k} \cdot \sigma_s)] \exp(-k^2/k_0^2) k dk d\theta, \quad (\text{A3})$$

where  $\theta$  is the angle between  $k$  and  $\sigma_s$ . Performing the integration gives

$$D_\phi = 4\pi^2 \lambda^2 r_e^2 C_N^2 \Delta D k_0^2 [1 - \exp(-k_0^2 \sigma_s^2 / 4)]. \quad (\text{A4})$$

One can see that when  $k_0 \sigma_s \gg 1$ , the exponential term becomes negligible and the wave structure function saturates at a constant value. We therefore only consider the scenario of  $k_0 \sigma_s \ll 1$ .

Combing Equation (A2),  $D_\phi$  can be written as

$$D_\phi = 2\pi^{3/2} r_e^2 \lambda^2 l_0^{-1} \sigma_s^2 \Delta D \delta n_e^2. \quad (\text{A5})$$

The diffractive length,  $\sigma_{\text{diff}}$ , is therefore given by

$$\sigma_{\text{diff}} = [2\pi^{3/2} r_e^2 \lambda^2 l_0^{-1} \Delta D \delta n_e^2]^{-1/2}. \quad (\text{A6})$$

Finally, following the assumptions introduced in Section 3 and considering Equations (35) and (36), the temporal broadening caused by a Gaussian spectrum is

$$\tau_{\text{sc}} = \frac{r_e^2 \lambda^4 D M^2}{4c\pi^{1/2}(1+z_0)^3} \left(\frac{\delta n_e}{n_e}\right)^2 f l_0^{-1}. \quad (\text{A7})$$